energy&fuels

pubs.acs.org/EF

Article

Hydration of Transitional Shale and Evolution of Physical Properties Constrained by Concurrent NMR and Acoustic Observations

Yong Li,* Lifu Xu, Jianqi Chen, Weiqi Zhang, and Derek Elsworth

Cite This: *Energy Fuels* 2023, 37, 7809−7822

Read Online

ACCESS | Metrics & More | Article Recommendations

ABSTRACT: Hydration state is a key factor affecting the pore structure and mechanical properties of shale that directly impacts the migration and then production of geofluids. We quantify the impact of the hydration state on physical properties through spontaneous imbibition experiments constrained by concurrent nuclear magnetic resonance (NMR) and acoustic observations as diagnostics of response. The long-duration experiments (24 days) are on samples from the Permian Shanxi Formation of the Ordos Basin, complemented by measurements of composition and physical properties. These shales primarily comprise quartz and clay minerals with intraparticle pores present within the clay minerals. The NMR T_2 spectra indicate that mesopores (2−50 nm) comprise ∼80% of the total pore space. The imbibition rate decreases by a factor of 3 from 0.08 g/h to a stable rate of 0.03 g/h from the 1st to the 24th hour. This is accompanied by a 10% decrease in the deformation modulus from 44 to 40.3 GPa over 24 days. The reduction in the modulus is consistent with observations of the shedding and spalling of hydrophilic quartz particles from the unconstrained surface and the generation of fractures. Reduction in the imbibition rate is consistent with the swelling followed by squeezing of clay minerals and the corresponding reduction in pore diameters in the confined core of the sample, together with the reduction in saturation gradients with the progress of imbibition. Understanding the mechanisms and effects of hydration on the pore structure and mechanical properties is important in understanding the shale hydration process and defining diagnostic (acoustic and NMR) signatures that may be used in reservoir surveillance.

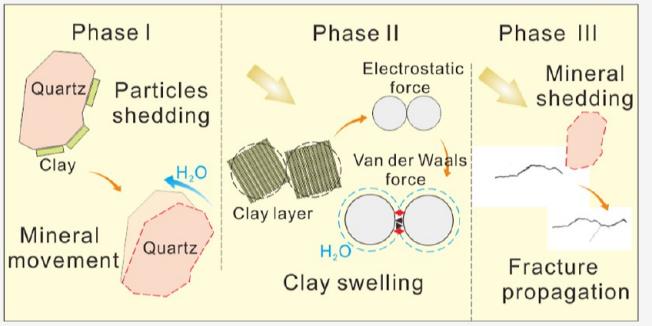

1. INTRODUCTION

Shale is an aggregate comprising clay and clastic minerals together with organic matter and serves as an important reservoir for natural gas and oil.[1−3] Natural gas is stored within micro- and nanopores in both free and adsorbed states; thus, apart from producing oil and gas, it is also an important reservoir for the storage of H_2 and for the sequestration of CO_2.[4−7] The imbibition of water is inevitable during the production of gas from shale, as aqueous fluids are ubiquitous in the many engineered interventions, viz, hydraulic fracturing.[8] Hydration is the infiltration of water into the mineral crystalline lattice of the mineral aggregate or the attachment of water molecules to the ions of soluble rocks, resulting in microscopic and macroscopic changes in the rock structure.[9,10] Hydration potentially decreases cohesion within the shale and alters the physical properties, which in turn impacts transport properties and rates of recovery of shale gas and oil.[11,12]

The main damage caused by hydration is the result of clay mineral swelling, dissolution, and the shedding of clastic particles.[13−15] Variations in the pore structure resulting from hydration mainly result from the dissolution of minerals and result in the dislodging of mineral particles and the concomitant enlargement of pores.[16,17] However, higher clay mineral contents may lead to pore blockage due to clast swelling and the concomitant pore shrinkage.[18,19] In addition, hydration reduces the strength of shale, which may exacerbate wellbore collapse or aid hydraulic fracturing.[20−22] Hydration may even generate micro-fractures and form complex fracture networks connecting micro- or nano-pores.[23−25] With the progress of hydration, micro-fractures will extend and connect, ultimately developing transmissive fracture systems.[23,26] Thus, hydration promotes changes in the pore structure and the physical characteristics of shales, manifest as changes in the porosity and permeability, with clay mineral type, hydration time, pH, and ionic composition of the water (i.e., different fracturing fluids) all impacting the response.[27−30] However, the detailed imbibition process and hydration damage on transitional shale has not been fully revealed.

Received: March 17, 2023
Revised: May 3, 2023
Published: May 15, 2023

https://doi.org/10.1021/acs.energyfuels.3c00899
Energy Fuels 2023, 37, 7809−7822

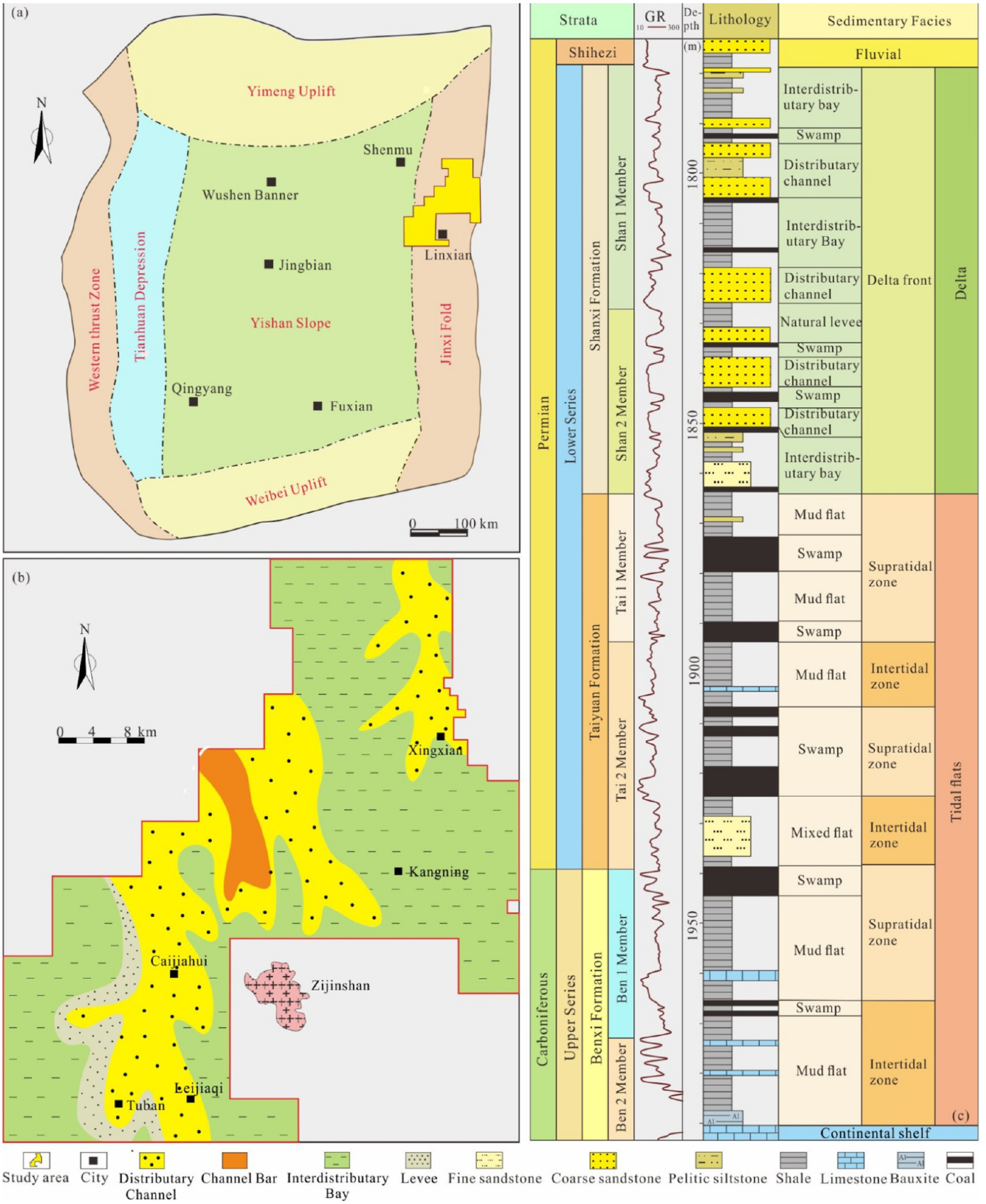

Figure 1. Geographical location and sedimentary environment of the study area. (a) Regional tectonics of the Ordos Basin. (b) Sedimentary environment distribution of Shanxi Formation in the Linxing area. (c) Carboniferous-Permian stratigraphy and sedimentary facies of the study area.

According to the analysis of hydration mechanism, the hydration damage of shale is related to the nature of shale itself and external conditions. Mineral composition and pore structure are intrinsic factors that affect the degree of hydration damage on shale, which directly influences the rate and degree of hydration. We systematically explore and quantify the influence

https://doi.org/10.1021/acs.energyfuels.3c00899
Energy Fuels 2023, 37, 7809−7822

Table 1. Basic Characteristics of the Shale Samples[a]

samples	lithology	depth (m)	length (cm)	diameter (cm)	mass (g)	TOC (wt %)	vitrinite reflectance (%)	T_{max} (°C)	kerogen type
C1	dark shale	1946.86	4.61	2.49	55.17	1.53	1.04	444	III
C2	dark shale	1947.70	4.99	2.50	67.23	2.01	1.07	449	III
C3	dark shale	1948.15	4.95	2.51	62.74	2.36	1.07	456	III
C4	dark shale	1949.54	4.71	2.50	61.52	2.54	1.10	453	III
C5	dark shale	1950.67	5.63	2.52	71.99	2.28	1.07	461	III
C6	dark shale	1951.58	5.15	2.52	64.92	3.12	1.12	460	III

[a]The temperature at the time of peak S_2 (the remaining generative source potential) evolution was recorded as T_{max}.

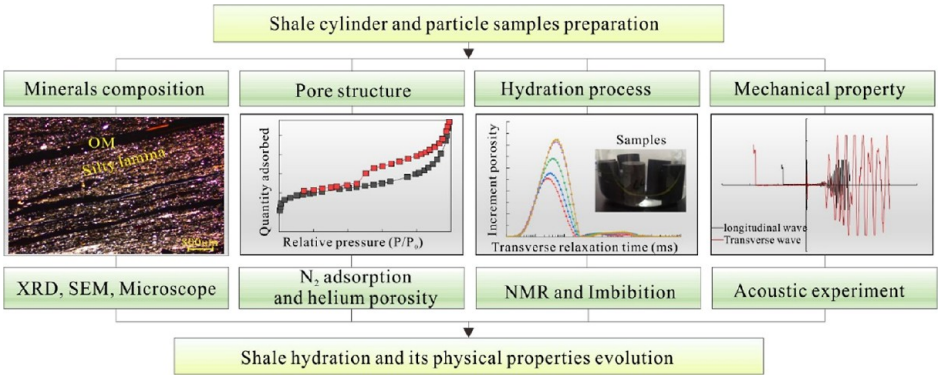

Figure 2. Schematic of the analytical protocol used in this shale hydration study.

of hydration on the evolution of physical properties in marine—continental transitional shale through a combination of various experiments. We complete long-term (24 days) imbibition experiments concurrently constrained by nuclear magnetic resonance (NMR) spectroscopy to determine the extent of water intrusion and its influences. The mineral composition and pore structure influences on the imbibition are also discussed. The ensemble results are beneficial to constrain active processes, define controls on hydration and process feedbacks, and provide discriminating diagnostics.

2. GEOLOGICAL SETTING

The Ordos Basin is located in the west of the North China Craton, which has six tectonic elements.[31] The basin experienced a large transgression regressive cycle in the late Paleozoic era and developed a set of thick marine−continental transitional coal-bearing deposits, which constituted the most important coal- and gas-bearing strata in the Ordos Basin, realizing the transformation from marine to continental deposits.[32] The sampling area is located in the north of the Jinxi Fold, on the eastern margin of the basin.[33] The marine−continental transitional shale is widely developed in the study area, mainly including the Carboniferous Benxi Formation, Permian Taiyuan Formation shale, and Shanxi Formation shale. The Shanxi Formation is mainly a delta sedimentary environment, while the Taiyuan and Benxi Formations are barrier islands, tidal flats, and lagoon sedimentary environments (Figure 1). The marine−continental transitional shale has good hydrocarbon generation potential, with the total organic carbon (TOC) content ranging from 1.44 to 7.1 wt %, which is in the mature to high mature stage with the organic matter type of mainly type III.[34] Meanwhile, the shale has typical characteristics of thin single-layer thickness, high clay mineral content (over 50%), and poor pore development.[35]

3. METHODOLOGY

3.1. Samples. A total of six samples of dark shales were recovered from a fresh well accessing the Permian Shanxi Formation in the northeastern Ordos Basin, China. Shale samples have good hydrocarbon generation potential (average TOC content of 2.31 wt %) and are in the mature stage (average vitrinite reflectance (R_o) of 1.08% and T_{max} of 454 °C), with organic matter type III, which represent the relatively high-quality marine−continental transitional shale. All samples were prepared as core plugs (Table 1) and were used to record the evolution of porosity and permeability via acoustic and NMR measurements throughout the concurrent imbibition of water. The remaining samples were ground to 200 mesh and 60−80 mesh powders for XRD and low-temperature nitrogen (N_2) adsorption measurements, respectively. All core samples were sealed before analysis to avoid oxidation, with all experiments conducted in the laboratory of CNOOC Ener Tech-Drilling & Production Co.

3.2. Experimental Section. As shown in Figure 2, the experimental design comprises the following: (1) Use low-temperature N_2 isothermal adsorption experiments, XRD, and porosity and permeability measurement, to define baseline parameters of the samples, including specific surface area (SSA), pore volume (PV), mineral composition, porosity, and permeability. (2) Oven-dry the core plugs at a low temperature (50 °C) for 12 h, measure the longitudinal and transverse wave velocities of the initial samples, and evaluate Young's modulus. (3) Measure the weight of the sample soaked in distilled water for 1 h, 3 h, 6 h, 12 h, 1 day, 3 days, 6 days, 10 days, and 12 days, and conduct NMR experiments after each weighing. (4) Then, dry the samples at a low temperature (50 °C) and remeasure the dynamic Young's moduli. (5) Evaluate the observed changes in material characteristics using process-based models.

3.2.1. XRD and Microscopic Observation. Whole rock XRD analysis was completed on 200 mesh powdered samples with mineral compositions recovered from a D/max-PC2600 X-ray

https://doi.org/10.1021/acs.energyfuels.3c00899
Energy Fuels 2023, 37, 7809−7822

Table 2. Mineral Composition and Pore Parameters of Samples[a]

	mineral compositions (wt %)						clay minerals (wt %)				pore parameters	
samples	quartz	potash feldspar	plagioclase	calcite	pyrite	clay	I	K	C	I/S	SSA (m^2/g)	PV (cm^3/g)
C1	51	1	3	0	3	42	39	31	9	21	14.00	0.0196
C2	30	0	1	0	1	68	44	20	3	33	9.04	0.0139
C3	39	1	4	0	13	43	38	36	8	18	8.25	0.0150
C4	31	1	7	0	2	59	27	23	4	46	7.87	0.0128
C5	39	1	1	1	13	45	95	2	2	1	12.91	0.0169
C6	37	1	4	0	14	44	39	35	8	18	8.25	0.0177

[a]I: illite; K: kaolinite; C: chlorite; I/S: illite and smectite mixed layer; SSA: specific surface area; PV: pore volume.

diffractometer at CNOOC, Tianjin. The D/Max-2600 X-ray diffractometer uses Cu Kα irradiation of the sample powder deposited on a glass substrate, with the irradiation angle varying from $2\theta = 2.5$ to 70° in 4° increments.

Thin sections were prepared on glass substrates (25 mm × 25 mm × 5 mm) ground to a thickness of 0.03 mm. The thin section observations were conducted with Leica DM4500p to identify the lithofacies.

3.2.2. Low-Temperature N_2 Adsorption Experiments. Low-pressure N_2 adsorption experiments were performed at 77.35 K on an ASAP2460 Surface Area Analyzer and Pore Size Analyzer. All samples were powdered to 60−80 mesh, dewatered at 110 °C for 5 h, then outgassed at 110 °C for 24 h[36] SSA were recovered from N_2 adsorption using the Brunauer−Emmett−Teller (BET) model with PV calculated using the Barrett−Joyner−Halenda (BJH) method following ISO 15901-2.[3]

3.2.3. Helium Porosity and Permeability. Porosity was determined using a Vinci porosity tester at a pressure of 104.1 kPa and temperature of 296.1 K. The gas permeability perpendicular to the bedding direction was measured by a Vinci permeability instrument. Permeability measurements on the shale core plugs were conducted at an effective stress of 3.44 MPa (500 psi). Experimental details and required calculations are reported in previous studies.[37−39]

3.2.4. Scanning Electron Microscopy. An FEI Quanta FEG 450 at the CNOOC facility in Tianjin was used to acquire high-resolution images of the distributions of the minerals and pores. Sub-samples with a diameter of 10 mm and thickness of 2−5 mm were cut from the shale samples. The sub-samples were prepared by ion polishing using a Gatan Ilion II broad beam argon milling system and coated with a 10−20 nm carbon film. The operating parameters were: working voltage 200 V to 30 kV, beam current up to 200 nA, and continuously adjustable. The high vacuum mode (chamber vacuum pressure < 6×10^{-4} Pa; nominal 1.0 nm electron beam resolution at 30 kV) was used for high-resolution imaging of shale samples in both secondary electron (SE) and backscattered (BSE) modes. By combining hundreds of high-resolution images into a single image (termed MAPS), the mineral and organic matter distributions could be simultaneously imaged.[3]

3.2.5. NMR Measurements. NMR measurements can detect signals of pore fluids in rock cores and have the characteristics of non-destructive, fast, and accurate detection.[40] A Mesomr 23-040h-1 nuclear magnetic resonance instrument was used, with a maximum radiofrequency (RF) pulse of 23 MHz and a minimum echo interval of 0.12 ms.

T_2 time is related to the pore radius (r) as[13]

$$\left(\frac{1}{T_2}\right)_{\text{total}} = \left(\frac{1}{T_2}\right)_{\text{s}} + \left(\frac{1}{T_2}\right)_{\text{D}} + \left(\frac{1}{T_2}\right)_{\text{B}} = \rho\left(\frac{S}{V}\right)_{\text{pore}} \quad (1)$$

$$\frac{S}{V} = \frac{F_{\text{s}}}{r} \quad (2)$$

$$r = (T_2)_{\text{s}} \cdot \rho \cdot F_{\text{s}} \quad (3)$$

where T_2 is the surface relaxation time (ms); $\left(\frac{1}{T_2}\right)_{\text{s}}$ is the surface relaxation contribution of the mineral grains; $\left(\frac{1}{T_2}\right)_{\text{D}}$ is the contribution of fluid relaxation; $\left(\frac{1}{T_2}\right)_{\text{B}}$ is the contribution of the internal molecular diffusion, where $\left(\frac{1}{T_2}\right)_{\text{D}}$ and $\left(\frac{1}{T_2}\right)_{\text{B}}$ are negligible; ρ is the surface transverse relaxation strength (μm/ms) with $\rho = 19.0542$ μm/s; S is the surface area of the pores (cm^2); V is the PV (cm^3); F_{s} is the shape factor of pores ($F_{\text{s}} = 3$, 2, and 1 for spherical pores, columnar pores, and slit pores, respectively); and r is the pore radius.

3.2.6. Acoustic Measurements. Acoustic wave−speed measurements are a common method to characterize the dynamic mechanical properties of materials.[41] Measurements were made using an E-hyfz-00081 scms-e rock acoustic characteristic tester at 25 °C and 30 MPa confining pressure. The dynamic Young's modulus was evaluated as[42]

$$E = \rho v_{\text{s}}^2 \left(\frac{3v_{\text{p}}^2 - 4v_{\text{s}}^2}{v_{\text{p}}^2 - v_{\text{s}}^2}\right) \quad (4)$$

where ρ is the density, g/cm^3; v_{p} is the longitudinal wave velocity, m/s; v_{s} is the transverse wave velocity, m/s; and E is the dynamic Young's modulus, GPa.

3.2.7. Imbibition Experiment. Before the experiment, the samples were dried at 105 °C until the mass remained unchanged. In the spontaneous imbibition experiment, each sample was completely immersed in distilled water. The mass change during the spontaneous imbibition was recorded until the mass became stable. To characterize the water absorption in the process of shale imbibition, the water content and imbibition rate were calculated as follows[43]

$$m(t) = \frac{m_t - m}{m} \quad (6)$$

$$v(t) = \frac{m_{t+1} - m_t}{t_{n+1} - t_n} \quad (7)$$

where $m(t)$ is the water content at each time during the shale imbibition process, %; with m_t as the wet weight at each time during imbibition, g; m as the dry weight of the sample before imbibition, g; and $v(t)$ represents the imbibition rate of shale, g/h; with $m_{t+1} - m_t$ representing the wet weight difference across a

https://doi.org/10.1021/acs.energyfuels.3c00899
Energy Fuels 2023, 37, 7809−7822

sampling interval in the imbibition process, g; $t_{n+1} - t_n$ is the duration of that sampling interval, h.

4. RESULTS

4.1. Mineral Composition. The dark shales mainly comprise quartz and clay minerals, with average contents of 38 and 50 wt %, respectively (Table 2). The shales also contain a small amount of feldspar, calcite, and pyrite (Table 2). The clay minerals are mainly illite (averaging 47 wt %), kaolinite (averaging 24.5 wt %), and illite−smectite mixed layers (averaging 22.8 wt %), with small amounts of chlorite. However, the relative content of illite in the clay mineral fraction of sample C5 is 95 wt %, far higher than that of other samples. Under an optical microscope, organic matter, argillaceous matter, and silty particles in the shale often have laminar distributions with sub-parallel laminar fractures (Figure 3a,b).

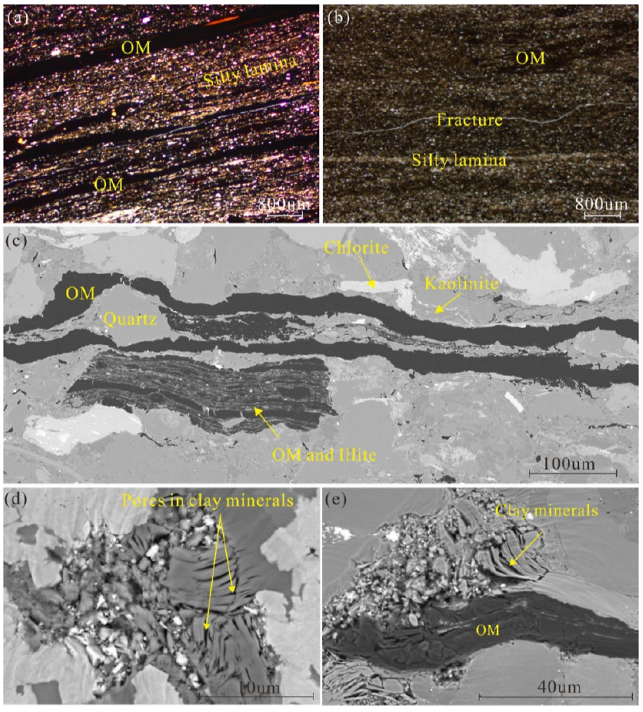

Figure 3. Multi-scale imaging of shale samples using different techniques: (a) sample C1: OM and silty particles distributed in laminae (optical microscopy); (b) sample C2: argillaceous and silty particles distributed in laminae (optical microscopy); (c) sample C1: distribution of OM and minerals (SEM); (d) sample C5: intraparticle pores within clay minerals (SEM); (e) sample C6: co-occurrences of clay minerals and OM (SEM). OM refers to organic matter.

4.2. Pore Structure and Pore Properties. SEM imaging shows that the organic matter is closely connected with clay minerals in the shale, especially as illite filled with organic matter (Figure 3c). Clastic minerals are dissolved and transformed into clay minerals with more intraparticle pores developed (Figure 3d). Organic matter, clay minerals, and clastic minerals often co-occur and influence each other (Figure 3e).

According to the IUPAC (International Union of Pure and Applied Chemistry) classification, the N_2 adsorption curves are mainly type IV, with hysteresis loops of types H_2−H_3 (Figure 4), indicating that the shales have widely developed slit pores and ink-bottle pores.[44] The adsorption and desorption curves of all samples are similar, but the average quantity of the adsorbed gas is higher in sample C5 than in all other samples (Figure 4e). The specific pore surface areas (from the BET method) of the samples range from 7.87 to 14.00 m^2/g, and the PV (from the BJH method) is 0.0128−0.0196 cm^3/g (Table 2). Since the nitrogen adsorption data indicate that there are a large number of slit pores in the samples, F_s is taken as 1 in the pore size conversion formula for the NMR data (eq 3). From this, if T_2 is less than 0.1072 ms then the pore is defined as a micropore (0−2 nm); T_2 between 0.1072 and 2.6561 represents a mesopore (2−50 nm); and T_2 greater than 2.6561 represents a macropore (>50 nm).

4.3. Imbibition Response. The water content and imbibition rates of shales change dynamically during imbibition. The imbibition process can be clearly divided into three stages (Table 3 and Figure 5): during the first stage of shale imbibition (<6 h), the wet weight and water content of samples increased rapidly, while the imbibition rate decreased rapidly. Over the second and intermediate stage (6 h−1 d), the shale was relatively saturated, the wet weight and water content increased more slowly, and the imbibition rate correspondingly decreased slowly. Finally, over the third stage (>1 d), the shale was saturated and the wet weight, water content, and imbibition rate fluctuated only slightly. However, the intrinsic heterogeneity of shales leads to differences of imbibition properties and behavior. For example, the mass of sample C2 changed only slightly during 6−12 h in the intermediate stage of imbibition compared to the other samples (Figure 5a), while the imbibition rate of sample C5 was the highest at 3 h, in contrast to the other samples, in which it was the highest after only 1 h (Figure 5b).

4.4. Variations in T_2 Spectra during Imbibition. NMR transverse relaxation times T_2 reflect pore diameters and porosity distributions of the shales.[45] The longer the transverse relaxation time, T_2, the larger the pore diameter. Furthermore, the larger the signal amplitude, the larger the PV.[26] As shown in Figure 6, the T_2 spectra of the initial samples show a bimodal distribution, indicating the presence of two independent pore systems. The first peak is in the range representing mesopores, and the second peak is in the range for macropores. Based on the distribution of the T_2 spectra, ~80% of the porosity in the shale samples is represented by mesopores, followed by the proportion of micropores then macropores (Table 4).

With increasing imbibition time, the T_2 spectra gradually present a trimodal or "triple peaked" distribution, with the third peak emerging in the macropore size range (Figures 6 and 7). Within 0−24 h, the magnitude of the first peak of the T_2 spectra increased and was significantly displaced to higher T_2 values and larger pores (Figure 6). The second peak of the T_2 spectra only showed a small variation in magnitude or value, except for the imbibition curve for sample C2 at 3 h (Figure 6b). The timing of the third peak of the T_2 spectra for samples C2, C3, and C5 varied significantly at 3, 12, and 3 h, respectively (Figure 6bc,e). However, the third peak of the T_2 spectra for sample C6 was extremely small (Figure 6f) over the entire first 24 h. After more than 1 day of imbibition, the T_2 spectra for samples C1, C2, C4, and C6 showed only small variations, while the third peak for sample C4 essentially disappeared. On the 10th day, the T_2 spectra of samples C3 and C5 shifted significantly to lower T_2 values, and fractures appeared on the end surfaces of C3 and C5, with C5 showing three staggered fractures (Figure 7c,e).

The changes in T_2 spectra show the dynamic process of water imbibition into different populations of pore diameters to the total porosity during the process of imbibition. During the imbibition process, the average contribution of micropores and

https://doi.org/10.1021/acs.energyfuels.3c00899
Energy Fuels 2023, 37, 7809−7822

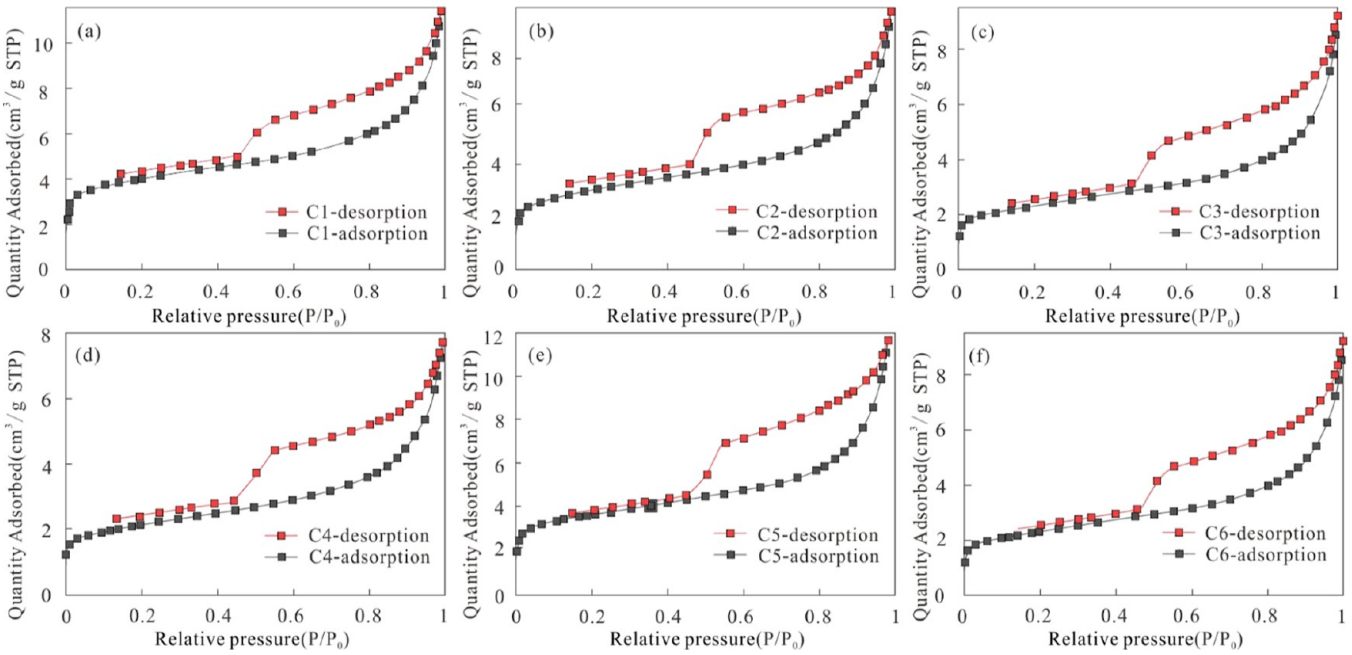

Figure 4. N_2 adsorption−desorption curves for shale samples [(a−f) samples C1 to C6, respectively].

Table 3. Variation in the Sample Mass during Shale Imbibition

		wet weight (g)								
samples	dry weight (g)	1 h	3 h	6h	12 h	1 d	3 d	6 d	12 d	24 d
C1	55.17	55.29	55.48	55.64	55.70	55.74	55.76	55.77	55.79	55.80
C2	67.02	67.08	67.16	67.18	67.18	67.23	67.27	67.28	67.28	67.28
C3	62.74	62.84	62.99	63.05	63.17	63.19	63.24	63.24	63.26	63.28
C4	61.52	61.56	61.60	61.61	61.63	61.69	61.75	61.76	61.76	61.76
C5	71.89	71.96	72.11	72.20	72.26	72.27	72.29	72.31	72.33	72.33
C6	64.92	65.01	65.09	65.18	65.28	65.32	65.40	65.41	65.41	65.41

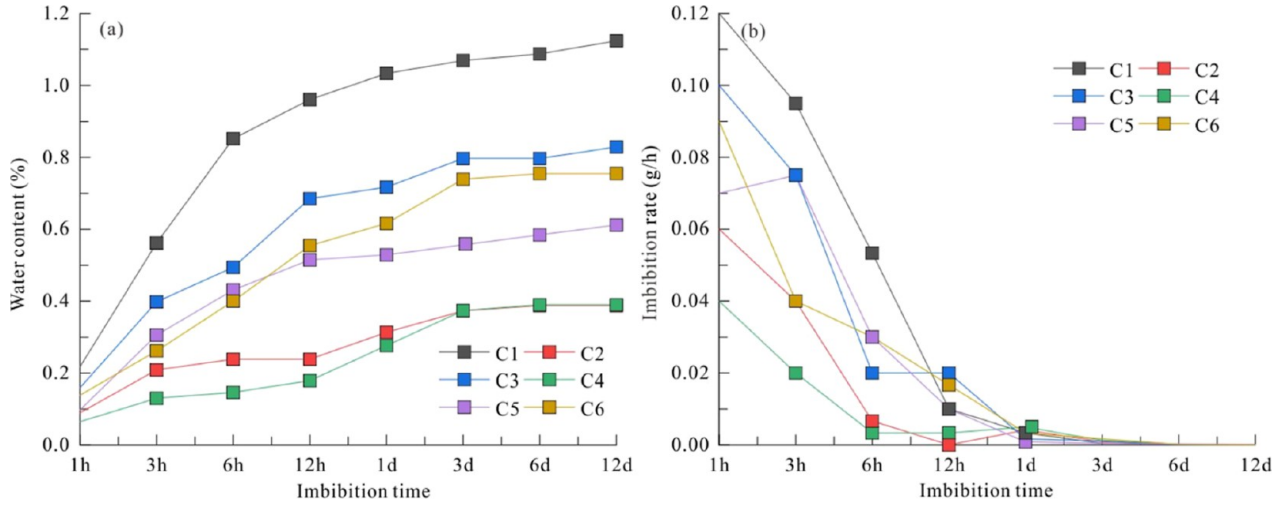

Figure 5. Variation in the water content (a) and imbibition rate (b) during shale imbibition.

macropores to the total porosity decreased from 13.8 to 10.2% and 8.4 to 5.8%, respectively, while that of mesopores increased from 77.8 to 84% (Table 4).

4.5. Effect of Imbibition on Mechanical Properties. The process of imbibition is often accompanied by hydration, which can have a significant impact on the mechanical properties of shale, especially when fracturing occurs in the sample during imbibition. Hydration fractures in shale may be partially closed under confining pressure.[29] To simulate the impact of in situ stresses, the longitudinal and transverse wave velocities of the samples were measured at a confining pressure of 30 MPa, and the dynamic Young's modulus was calculated. The average dynamic Young's modulus of the shale decreased from 44 to

https://doi.org/10.1021/acs.energyfuels.3c00899
Energy Fuels 2023, 37, 7809−7822

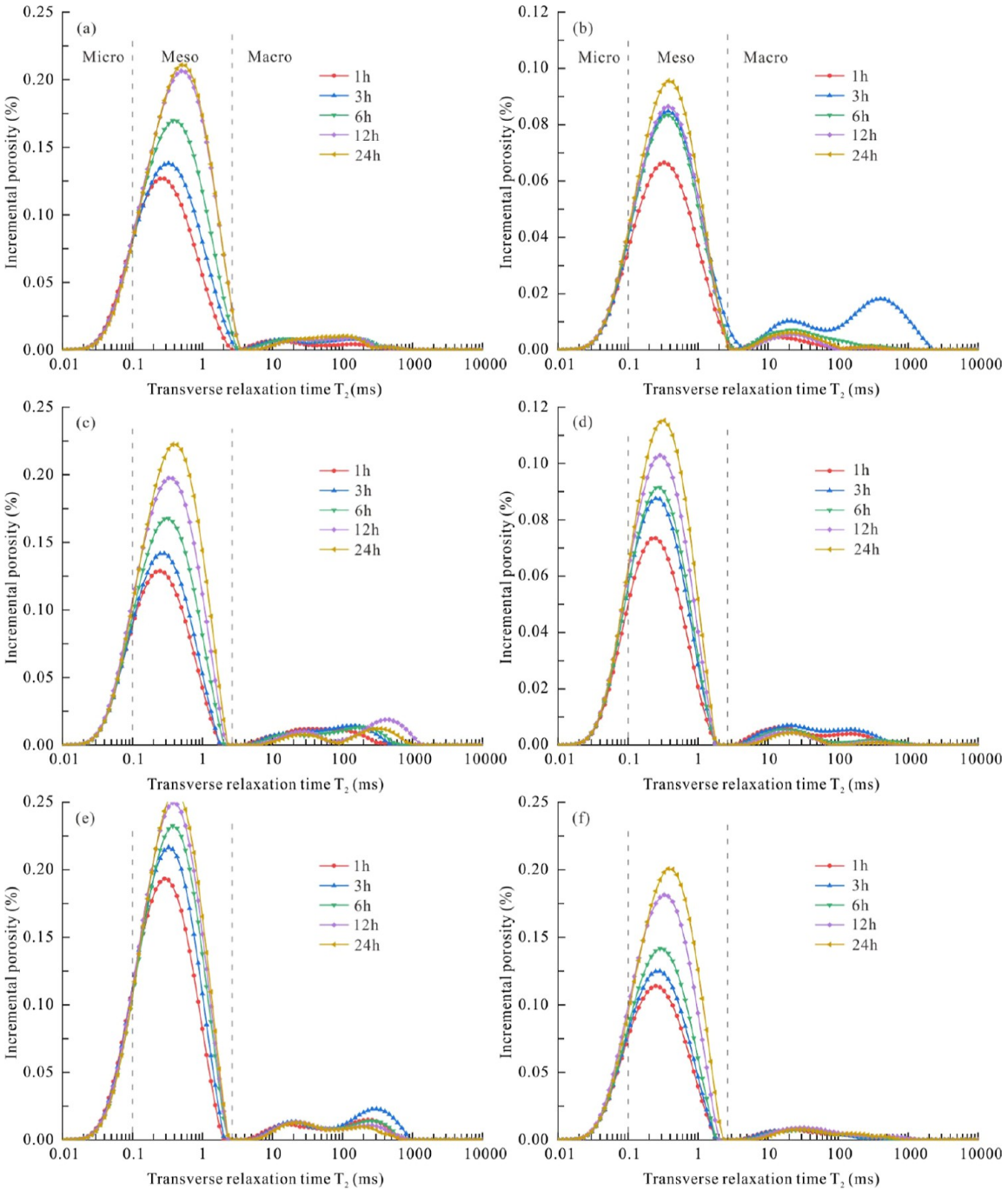

Figure 6. Distribution of T_2 spectra from 1 to 24 h of imbibition [(a–f) samples C1 to C6, respectively].

Table 4. Changes in Reservoir Parameters Both Pre- and Post-shale Imbibition

	before imbibition						after imbibition				
samples	porosity (%)	permeability (mD)	micropore (%)	mesopore (%)	macropore (%)	Young's modulus (GPa)	porosity (%)	micropore (%)	mesopore (%)	macropore (%)	Young's modulus (GPa)
C1	1.2	0.17	14.2	79.7	6.1	41.7	5.3	9.3	82.4	8.3	35.6
C2	0.8	0.02	10.8	83.1	6.1	58.5	2.0	9.0	85.0	6.1	57.0
C3	1.2	1.17	15.1	73.9	11.0	38.5	4.9	10.0	84.4	5.6	33.2
C4	0.8	0.01	15.3	74.4	10.3	44.3	2.5	12.1	83.8	4.1	41.9
C5	1.1	0.84	12.6	78.2	9.2	41.7	5.4	9.9	83.6	6.5	38.6
C6	1.1	0.40	15.1	77.3	7.6	39.2	4.1	11.2	84.8	4.0	35.7

https://doi.org/10.1021/acs.energyfuels.3c00899
Energy Fuels 2023, 37, 7809−7822

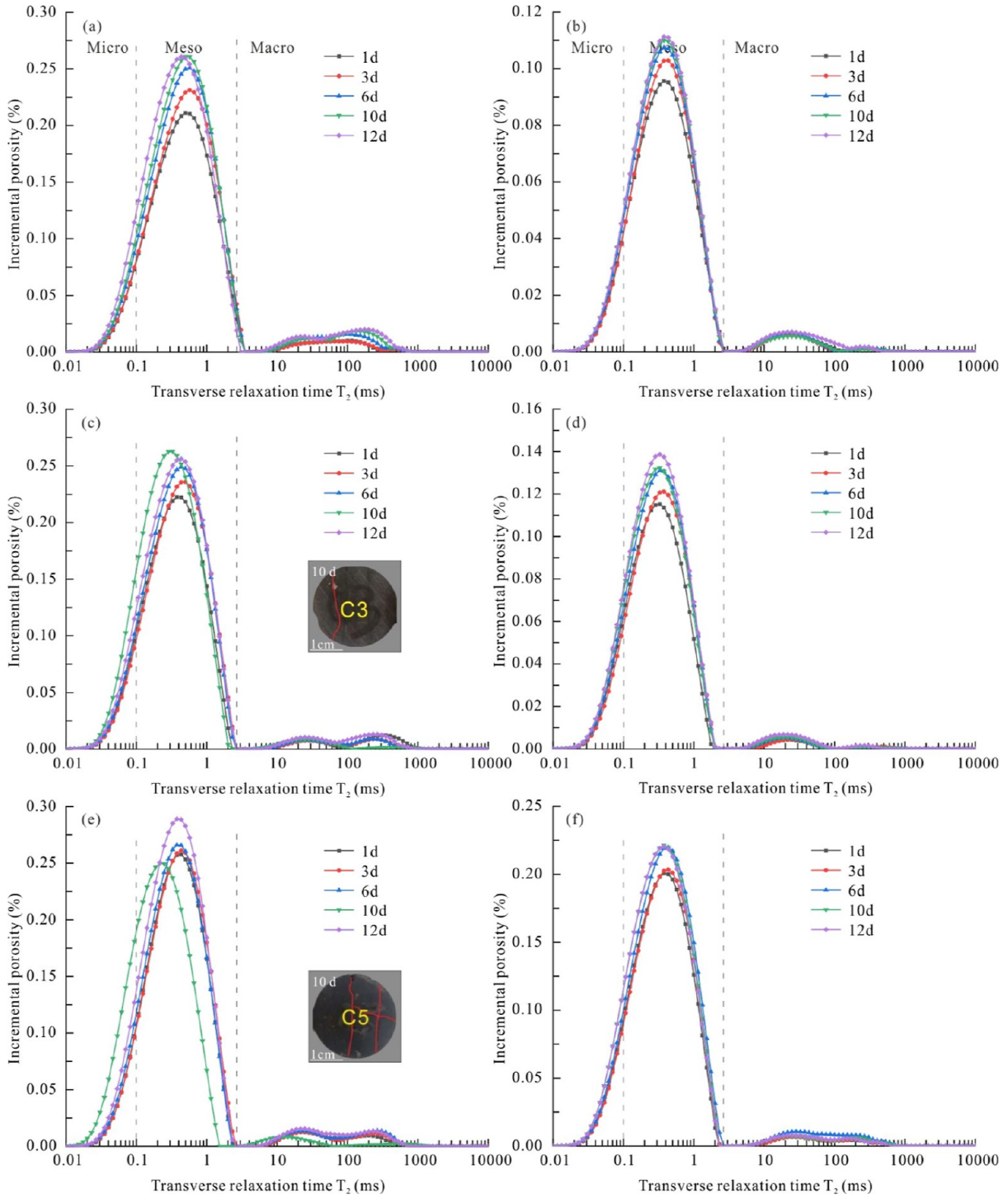

Figure 7. Distribution of T_2 spectra from day 1 to day 12 of imbibition [(a–f) samples C1 to C6, respectively].

40.3 GPa, indicating the impact of hydration in fracturing (Figure 8 and Table 4).

5. DISCUSSION

5.1. Controls on Imbibition Rate. The early stage of imbibition is characterized by high rates—resulting from the high saturation and capillary pressure gradients in the unsaturated sample. The initial imbibition rate (t = 1 h) has a significant positive correlation with the initial porosity (Figure 9). With an increase in the water saturation within the shale, the capillary pressure difference equilibrates and the driving pressure gradient gradually diminishes. However, water continues to migrate within the shale under the action of remnant capillary gradients and electrostatic forces. In addition to porosity, the initial imbibition rates of the samples are also related to pore connectivity and related permeability. For example, the initial porosity of sample C4 is larger than that of sample C2, but the initial imbibition rate of C4 is the lowest among all samples. This observation suggests that the permeability and pore connectivity of sample C4 is low compared to the other samples (Table 4).

https://doi.org/10.1021/acs.energyfuels.3c00899
Energy Fuels 2023, 37, 7809−7822

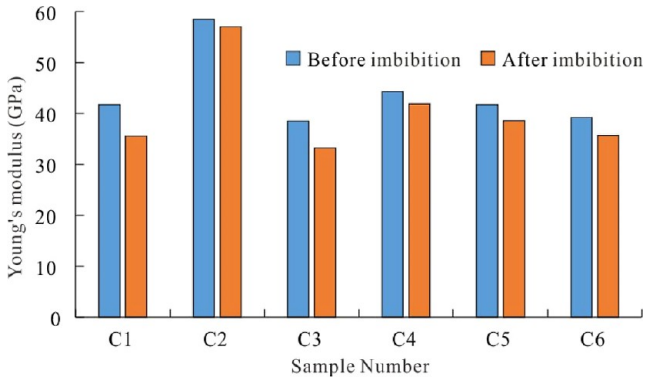

Figure 8. Variation in the dynamic Young's modulus of shale both pre- and post-imbibition.

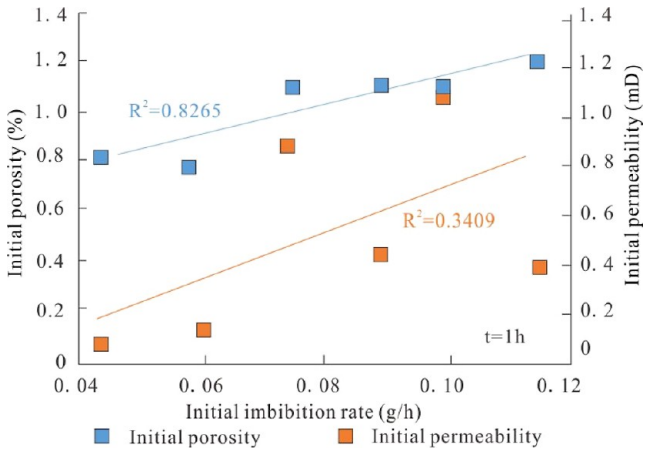

Figure 9. Relationship between initial porosity and permeability of shale samples and initial imbibition rates.

The initial imbibition rates (t = 1−6 h) are positively correlated with the quartz content but have no clear correlation with illite and illite−smectite mixed layer contents (Figure 9a−i). Because quartz particles are hydrophilic and exhibit intergranular pore connectivity, they provide adequate channels for fluid flow and enhance imbibition.[46,47] However, illite−smectite mixed layer clays may fill the intergranular pores and inhibit the fluid flow at an early time. With extended imbibition times, the hydration-driven expansion of clay minerals increases.[37,48] The expansion rate of smectite is lower than that of illite,[15] but the hydrogen bonds formed by the free hydroxyl and self-associated hydroxyl of illite are stronger than those of smectite, resulting in a lower expansion rate of illite. The imbibition rate of sample C5 is lower than that of C3 and C6 over the early experimental stages, but the differences in the imbibition rate are gradually inverted with increasing imbibition times. Because the illite content of sample C5 is high (95%), its imbibition rate over the first 3 h is large. However, the expansion rate of illite is low, and the squeezing effect on pores in the later stage of hydration is not readily apparent. Within 6−12 h, the imbibition rate becomes unrelated to the quartz content but still has a weak negative correlation with the presence of the illite−smectite mixed layer (Figure 10j−l), indicating that the water-absorption-driven expansion of the illite−smectite layers still continues. By 12−24 h, the imbibition rate of the shale has slowed and only has a significant positive correlation with the illite−smectite mixed layer (Figure 10m−o), indicating that the illite−smectite mixed layer is still absorbing water. Within 1−3 days, there is no obvious correlation between the shale imbibition rate and mineral composition, indicating that the samples have reached full saturation (Figure 10p−r).

In addition to the type and content of minerals, the mineral assemblages also affect the process of water intrusion. The C1 sample with a directional arrangement of clay minerals has the highest water absorption capacity and the highest imbibition rate in the early stage (Figures 3c and 5), indicating that a strong mineral arrangement can promote the imbibition process.[49] At the same time, the expansion of clay minerals in the early stage by water absorption can inhibit imbibition, while in the later stage, after the formation of water films, the debris particles may fall off and promote the imbibition (Figure 10).

5.2. Controls on Shale Mechanical Properties. Mineral composition, porosity, and pore structure exert a strong influence on the anisotropy of the mechanical properties of shales. The variation in the dynamic Young's modulus (Figure 11; reduction before and after hydration) has a strong positive correlation with the initial porosity (R^2 of 0.78), followed by PV (R^2 of 0.44), but has an insignificant correlation with permeability and initial SSA. Higher porosity will reduce the dynamic Young's modulus.[50] The shale is predominantly composed of quartz and clay minerals, and these determine the mechanical properties. The variation in Young's modulus is positively correlated with the concentrations of quartz (R^2 = 0.80) and negatively correlated with clay minerals (R^2 of 0.68) (Figure 11e,f). The drag forces generated during the imbibition of fluid into the pore system dislodge and displace quartz particles, with the net result that the number of micropores between clastic minerals and clay minerals decreases.[51] As a water film inhabits the surface of clay minerals, cements will dissolve and some quartz particles may spall and be shed from the grains.[16] Meanwhile, fractures will be formed as the pores between quartz grains are connected. The clay minerals in the clay layers will expand after contacting water, which will cause interlayer expansion, deformation, and compression of the intergranular pores of the clastic (non-clay) layers.[10] The clay minerals swell after absorbing water, and this swelling will counter the compaction and stiffen the skeleton. Thus, imbibition may significantly impact the reservoir matrix structure and thereby the mechanical properties of shales, which is consistent with previous research results.[52,53]

5.3. Shale Imbibition Model. Initial imbibition rates are high as capillary pressure gradients and out-of-balance electrostatic forces are high. This slows as water completely fills the pores, although the imbibition process proceeds dynamically, but is mainly due to hydration during the imbibition process. The pore structure of sample C5 changed on the 10th day of imbibition, and the contribution proportion of micropores to porosity increased significantly. This may have been the result of the fracturing process generating more micropores. Alternatively, some of the original closed micropores were destroyed (Figure 7e). Hydration not only affects the properties of minerals but also produces new fractures, leading to changes in the pore structure of shale and affecting the mechanical properties of the reservoir.[54]

The mineral composition of shales affects hydration in three main ways. The impact of clay mineral hydration and swelling on the pore structure is reflected in two aspects: first, cation exchange occurs during the contact between clay minerals and water, and the remaining negatively charged structural units in clay minerals. The separation of charged layers occurs due to electrostatic repulsion, which directly increases the number/

https://doi.org/10.1021/acs.energyfuels.3c00899
Energy Fuels 2023, 37, 7809−7822

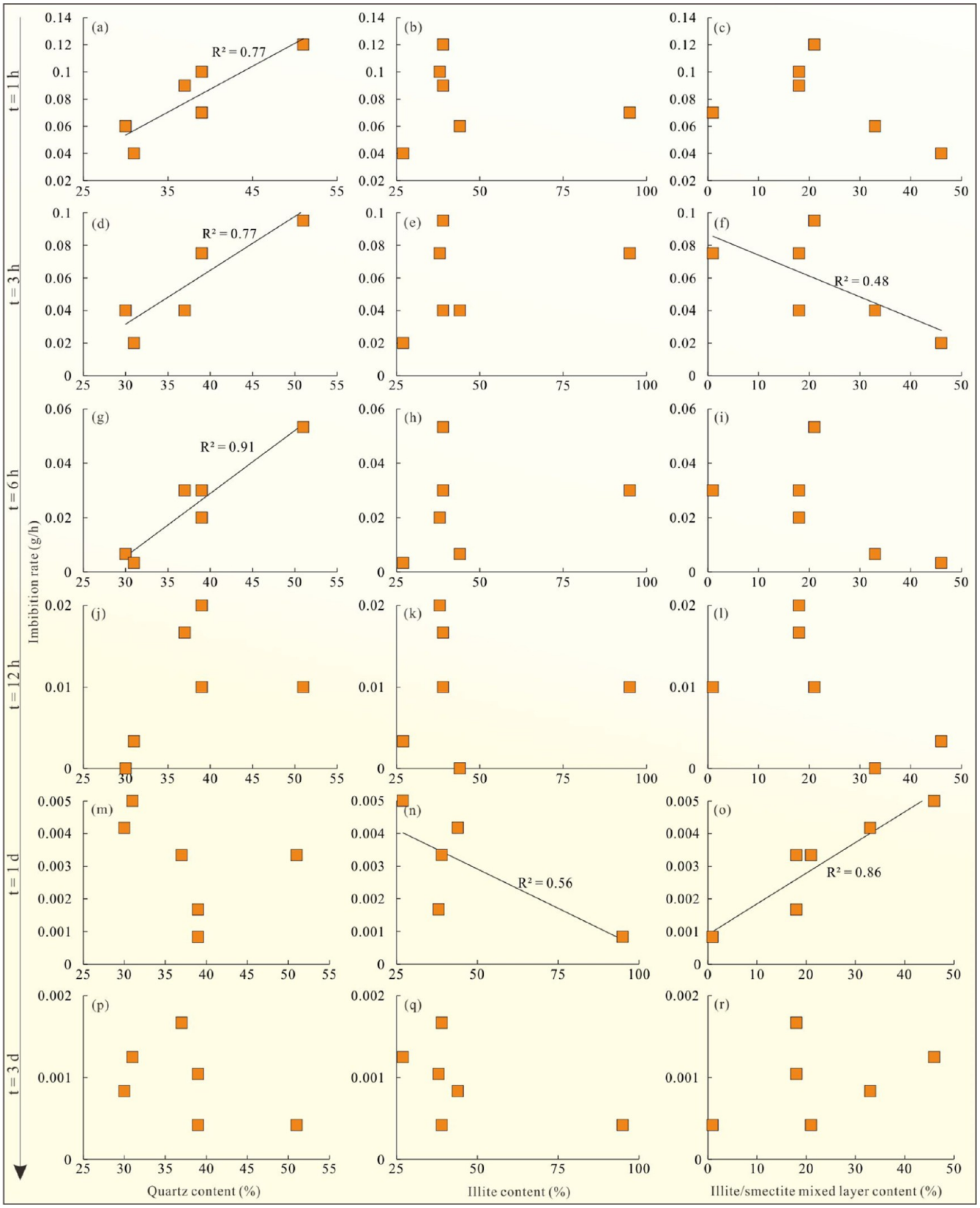

Figure 10. Correlation analysis between mineral compositions and imbibition rates.

volume of pores between clay mineral layers.[55] Second, when water contacts the clay minerals, it is adsorbed on the surface of the clay minerals by electrostatic forces and chemical bonding, eventually forming a hydrated film.[56] In the early stage of imbibition, clay mineral particles are transported during the dynamic flow of shale pore water, and shale deformation is obvious.[57] The feldspar and carbonate minerals are subject to dissolution when in contact with water for a prolonged period,

https://doi.org/10.1021/acs.energyfuels.3c00899
Energy Fuels 2023, 37, 7809−7822

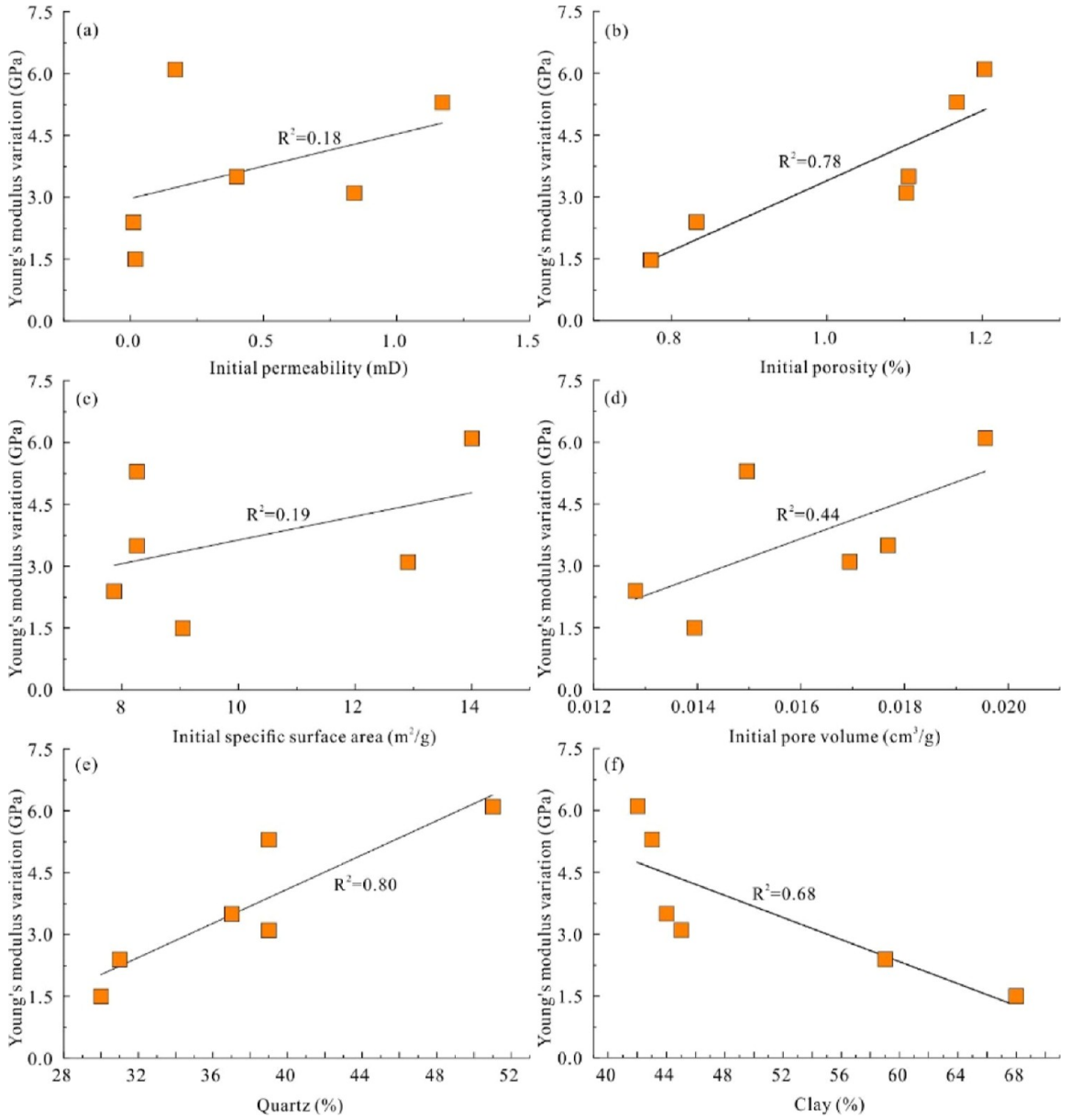

Figure 11. Relation between pore structural and physical properties to Young's modulus.

mainly related to the pH of the fluid.[58,59] However, the feldspar and carbonate contents of this shale are extremely low, and mineral dissolution is not apparent.

As a result, the main factors controlling the evolution of the pore structure in shales during imbibition can be divided into three stages. In the first stage, fluid enters the shale under the action of pressure differential and capillary forces, and the main influence on the pore structure is the viscous shear force applied by the fluid (Figure 12a). During this phase, small particles of clay are transported, clastic grains such as those of quartz are displaced, and intergranular pores between particles are enlarged (Figure 12b). In the second stage, the swelling of clay minerals such as layered illite−smectites increases the crystal spacing after absorbing water (Figure 12b). In the third stage, a water film is formed on the surface of the clay minerals after water absorption, which reduces the cementation of clay minerals and induces the shedding of quartz grains (Figure 12c), resulting in an increase in the number of pores. Meanwhile, hydration fractures are nucleated and extended, which reduces the Young's modulus (Figure 12d).

6. CONCLUSIONS

(1) During spontaneous imbibition, the initial imbibition rate has a positive correlation with porosity, suggesting that the connectivity of pores promotes this imbibition. In addition, hydrophilicity combined with adequate pore connectivity within the quartz promotes this imbibition, while the swelling of clay minerals counters this effect by inhibiting the imbibition.

(2) According to the T_2 spectra, the mesopores in the shale represent ~80% of the porosity. Moreover, the change in the relative proportions of micropores, mesopores, and macropores shows the influence of hydration on quartz, clay minerals, and fractures in the process of imbibition, which alters the pore structure of shale.

https://doi.org/10.1021/acs.energyfuels.3c00899
Energy Fuels 2023, 37, 7809−7822

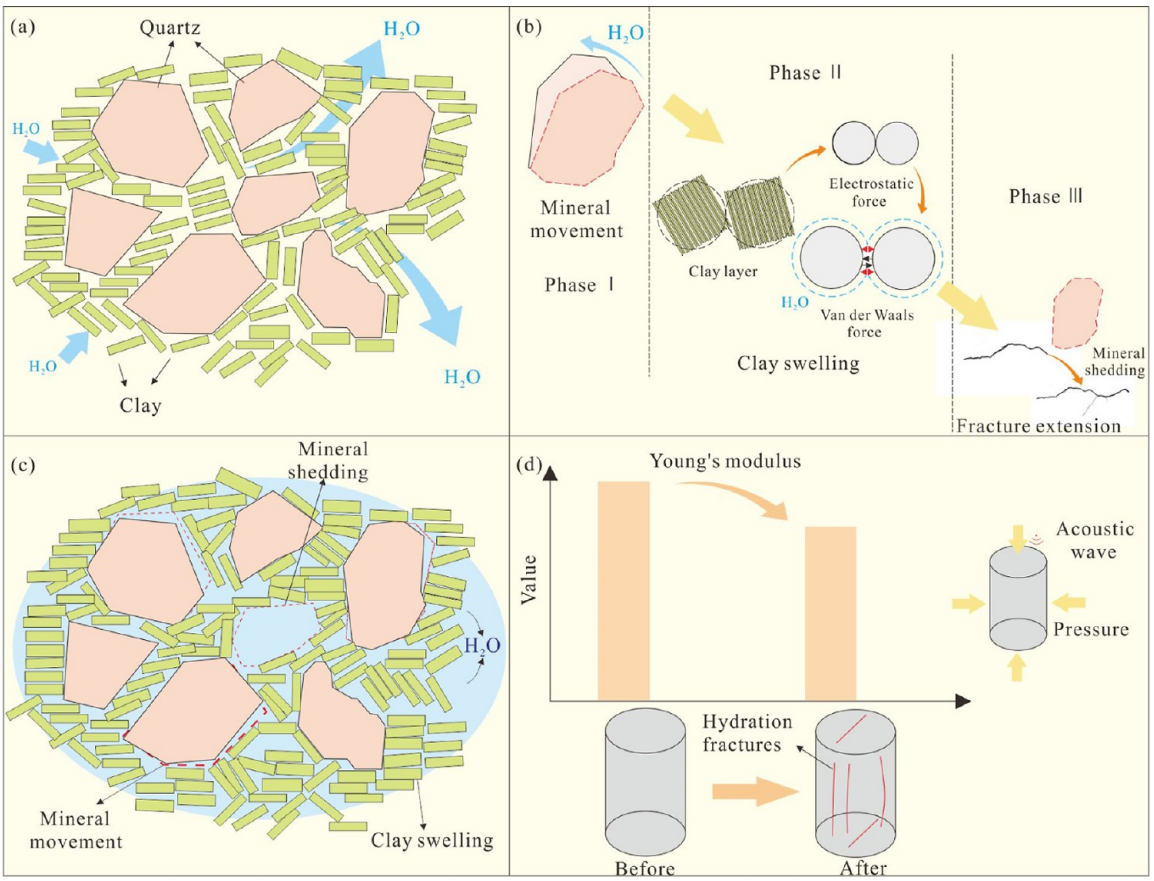

Figure 12. Schematic of progression of processes driving hydration. (a) Water enters the pores in shale; (b) pore evolution stage during imbibition; (c) hydration results in quartz particles being shed; (d) damage resulting in reduction in Young's modulus.

(3) The important influence of shale hydration on the physical characteristics of the reservoir is reflected in the change in the Young's modulus decreasing from 44 GPa pre-imbibition to 40.3 GPa post-imbibition. This variation in Young's modulus is related to the shedding of quartz particles, the expansion of clay minerals, and the generation of fractures. Based on these observations, the impacts of hydration on reservoir characteristics are established, potentially enabling acoustic measurements to be used as diagnostics in reservoir management.

(4) The main factors controlling the evolution of the pore structure in shales during imbibition can be divided into three stages. Fluid entry causes minerals rearrangement, detachment, expansion, and also new fractures, affecting the mechanical properties of the reservoir. For different types of shale, the effect of hydration on the reservoir and the stage of pore evolution is basically consistent, even though they are influenced by different minerals composition and diagenesis stages.

AUTHOR INFORMATION

Corresponding Author

Yong Li − *State Key Laboratory of Coal Resources and Safe Mining, College of Geosciences and Surveying Engineering, China University of Mining and Technology, Beijing 100083, China*; orcid.org/0000-0001-8859-156X; Email: liyong@cumtb.edu.cn, cugbliyong@gmail.com

Authors

Lifu Xu − *State Key Laboratory of Coal Resources and Safe Mining, College of Geosciences and Surveying Engineering, China University of Mining and Technology, Beijing 100083, China*

Jianqi Chen − *CNOOC EnerTech-Drilling & Production Co., Tianjin 300457, China*

Weiqi Zhang − *State Key Laboratory of Coal Resources and Safe Mining, College of Geosciences and Surveying Engineering, China University of Mining and Technology, Beijing 100083, China*

Derek Elsworth − *Department of Energy and Mineral Engineering, Geosciences, EMS Energy Institute and the G3 Center, Pennsylvania State University, University Park, Pennsylvania 16802, United States*

Complete contact information is available at: https://pubs.acs.org/10.1021/acs.energyfuels.3c00899

Notes

The authors declare no competing financial interest.

ACKNOWLEDGMENTS

This study was supported by the National Natural Science Foundation of China (grant no. 42072194, U1910205) and the Fundamental Research Funds for the Central Universities (800015Z1190, 2021YJSDC02).

REFERENCES

(1) Loucks, R. G.; Reed, R. M.; Ruppel, S. C.; Hammes, U. Spectrum of pore types and networks in mudrocks and a descriptive classification for matrix-related mudrock pores. *AAPG Bull.* **2012**, *96*, 1071−1098.

(2) Gaines, R. R.; Hammarlund, E. U.; Hou, X.; Qi, C.; Gabbott, S. E.; Zhao, Y.; Peng, J.; Canfield, D. E. Mechanism for Burgess Shale-type preservation. *Proc. Natl. Acad. Sci. U.S.A.* **2012**, *109*, 5180−5184.

(3) Li, Y.; Zhang, C.; Tang, D.; Gan, Q.; Niu, X.; Wang, K.; Shen, R. Coal pore size distributions controlled by the coalification process: An experimental study of coals from the Junggar, Ordos and Qinshui basins in China. *Fuel* **2017**, *206*, 352−363.

(4) Bustin, R. M.; Bustin, A. M.; Cui, A.; Ross, D.; Pathi, V. M. Impact of shale properties on pore structure and storage characteristics. In *SPE shale gas production conference*; OnePetro, 2008.

(5) Jarvie, D. M.; Hill, R. J.; Ruble, T. E.; Pollastro, R. M. Unconventional shale-gas systems: The Mississippian Barnett Shale of north-central Texas as one model for thermogenic shale-gas assessment. *AAPG Bull.* **2007**, *91*, 475−499.

(6) Zou, C.; Dong, D.; Wang, S.; Li, J.; Li, X.; Wang, Y.; Li, D.; Cheng, K. Geological characteristics and resource potential of shale gas in China. *Petrol. Explor. Dev.* **2010**, *37*, 641−653.

(7) Stephenson, M. H. Shale gas in North America and Europe. *Energy Sci. Eng.* **2016**, *4*, 4−13.

(8) Wang, F.; Pan, Z. Numerical simulation of chemical potential dominated fracturing fluid flowback in hydraulically fractured shale gas reservoirs. *Petrol. Explor. Dev.* **2016**, *43*, 1060−1066.

(9) Wu, Y. Mechanism analysis of hazards caused by the interaction between groundwater and geo-environment. *Eng. Geol.* **2003**, *44*, 811−819.

(10) Xue, H.; Ding, G.; Dong, Z.; Zhao, R.; An, C.; Li, B.; Zhou, Y.; Yan, P.; Yan, J.; Li, C.; Jin, Y. Study on the Wettability and Spontaneous Imbibition Characteristics of Lacustrine Shale. *Geofluids* **2022**, *2022*, 1−14.

(11) Dehghanpour, H.; Lan, Q.; Saeed, Y.; Fei, H.; Qi, Z. Spontaneous Imbibition of Brine and Oil in Gas Shales: Effect of Water Adsorption and Resulting Microfractures. *Energy Fuels* **2013**, *27*, 3039−3049.

(12) Roshan, H.; Ehsani, S.; Marjo, C. E.; Andersen, M. S.; Acworth, R. I. Mechanisms of water adsorption into partially saturated fractured shales: An experimental study. *Fuel* **2015**, *159*, 628−637.

(13) Hu, Y.; Zhao, C.; Zhao, J.; Wang, Q.; Zhao, J.; Gao, D.; Fu, C. Mechanisms of fracturing fluid spontaneous imbibition behavior in shale reservoir: A review. *J. Nat. Gas Sci. Eng.* **2020**, *82*, 103498.

(14) Zhang, Q.; Fan, X.; Chen, P.; Ma, T.; Zeng, F. Geomechanical behaviors of shale after water absorption considering the combined effect of anisotropy and hydration. *Eng. Geol.* **2020**, *269*, 105547.

(15) Liu, J.; Yang, Z.; Sun, J.; Dai, Z.; Lv, K.; You, Q. Experimental investigation on hydration mechanism of Sichuan shale (China). *J. Pet. Sci. Eng.* **2021**, *201*, 108421.

(16) Khan, H. J.; Spielman-Sun, E.; Jew, A. D.; Bargar, J.; Kovscek, A.; Druhan, J. L. A Critical Review of the Physicochemical Impacts of Water Chemistry on Shale in Hydraulic Fracturing Systems. *Environ. Sci. Technol.* **2021**, *55*, 1377−1394.

(17) Li, Q.; Li, J.; Zhu, B. Experimental investigation of the influence of sequential water-rock reactions on the mineral alterations and porosity evolution of shale. *Constr. Build. Mater.* **2022**, *317*, 125859.

(18) Muhammed, N. S.; Olayiwola, T.; Elkatatny, S. A review on clay chemistry, characterization and shale inhibitors for water-based drilling fluids. *J. Pet. Sci. Eng.* **2021**, *206*, 109043.

(19) Muhammed, N. S.; Olayiwola, T.; Elkatatny, S.; Haq, B.; Patil, S. Insights into the application of surfactants and nanomaterials as shale inhibitors for water-based drilling fluid: A review. *J. Nat. Gas Sci. Eng.* **2021**, *92*, 103987.

(20) Al-Arfaj, M. K.; Amanullah, M.; Sultan, A. S.; Hossain, E.; Abdulraheem, A. Chemical and Mechanical Aspects of Wellbore Stability in Shale Formations: A Literature Review. In *Abu Dhabi International Petroleum Exhibition and Conference*, 2014; D031S049R004.

(21) Liu, Z.; Sun, Y.; Guo, W.; Li, Q. Reservoir-scale study of oil shale hydration swelling and thermal expansion after hydraulic fracturing. *J. Pet. Sci. Eng.* **2020**, *195*, 107619.

(22) Mao, L.; Lin, H.; Cai, M.; Zhang, J. Wellbore stability analysis of horizontal wells for shale gas with consideration of hydration. *J. Energy Resour. Technol.* **2022**, *144*, 113003.

(23) You, L.; Zhou, Y.; Kang, Y.; Yang, B.; Cui, Z.; Cheng, Q. Fracturing fluid retention in shale gas reservoirs: mechanisms and functions. *Arabian J. Geosci.* **2019**, *12*, 779.

(24) Zeng, F.; Zhang, Q.; Guo, J.; Zeng, B.; Zhang, Y.; He, S. Mechanisms of shale hydration and water block removal. *Petrol. Explor. Dev.* **2021**, *48*, 752−761.

(25) Zeng, F.; Zhang, Y.; Guo, J.; Zhang, Q.; Chen, Z.; Xiang, J.; Zheng, Y. Optimized completion design for triggering a fracture network to enhance horizontal shale well production. *J. Pet. Sci. Eng.* **2020**, *190*, 107043.

(26) Wang, G.; Han, D.; Qin, X.; Liu, Z.; Liu, J. A comprehensive method for studying pore structure and seepage characteristics of coal mass based on 3D CT reconstruction and NMR. *Fuel* **2020**, *281*, 118735.

(27) Kang, Y.; Yang, B.; Li, X.; Yang, J.; You, L.; Chen, Q. Quantitative characterization of micro forces in shale hydration and field applications. *Petrol. Explor. Dev.* **2017**, *44*, 328−335.

(28) Tan, J.; Hu, C.; Lyu, Q.; Feng, G.; Chen, S. Experimental investigation on the effects of different fracturing fluids on shale surface morphology. *J. Pet. Sci. Eng.* **2022**, *212*, 110356.

(29) Zhang, S.; Sheng, J. J. Effect of Water Imbibition on Fracture Generation in Mancos Shale under Isotropic and Anisotropic Stress Conditions. *J. Geotech. Geoenviron. Eng.* **2018**, *144*, 04017113.

(30) Zhou, T.; Zhang, S.; Yang, L.; Ma, X.; Zou, Y.; Lin, H. Experimental investigation on fracture surface strength softening induced by fracturing fluid imbibition and its impacts on flow conductivity in shale reservoirs. *J. Nat. Gas Sci. Eng.* **2016**, *36*, 893−905.

(31) Ju, W.; Shen, J.; Qin, Y.; Meng, S.; Wu, C.; Shen, Y.; Yang, Z. B.; Li, G. Z.; Li, C. In-situ stress state in the Linxing region, eastern Ordos Basin, China: implications for unconventional gas exploration and production. *Mar. Pet. Geol.* **2017**, *86*, 66−78.

(32) Zhang, L.; Dong, D.; Qiu, Z.; Wu, C.; Zhang, Q.; Wang, Y.; Liu, D.; Deng, Z.; Zhou, S.; Pan, S. Sedimentology and geochemistry of Carboniferous-Permian marine-continental transitional shales in the eastern Ordos Basin, North China. *Palaeogeogr., Palaeoclimatol., Palaeoecol.* **2021**, *571*, 110389.

(33) Li, Y.; Wang, Z.; Wu, P.; Gao, X.; Yu, Z.; Yu, Y.; Yang, J. Organic geochemistry of Upper Paleozoic source rocks in the eastern margin of the Ordos Basin, China: Input and hydrocarbon generation potential. *J. Pet. Sci. Eng.* **2019**, *181*, 106202.

(34) Dong, D.; Wang, Y.; Li, X.; Zou, C.; Guan, Q.; Zhang, C.; Huang, J.; Wang, S.; Wang, H.; Liu, H.; Bai, W.; Liang, F.; Lin, W.; Zhao, Q.; Liu, D.; Qiu, Z. Breakthrough and prospect of shale gas exploration and development in China. *Nat. Gas Ind. B.* **2016**, *3*, 12−26.

(35) Kuang, L.; Dong, D.; He, W.; Wen, S.; Sun, S.; Li, S.; Qiu, Z.; Liao, X.; Li, Y.; Wu, J.; Zhang, L.; Shi, Z.; Guo, W.; Zhang, S. Geological characteristics and development potential of transitional shale gas in the east margin of the Ordos Basin, NW China. *Petrol. Explor. Dev.* **2020**, *47*, 471−482.

(36) Yang, F.; Hu, B.; Xu, S.; Meng, Q.; Krooss, B. M. Thermodynamic characteristic of methane sorption on shales from oil, gas, and condensate windows. *Energy Fuels* **2018**, *32*, 10443−10456.

(37) Tian, H.; Pan, L.; Xiao, X.; Wilkins, R. W. T.; Meng, Z.; Huang, B. A preliminary study on the pore characterization of Lower Silurian black shales in the Chuandong Thrust Fold Belt, southwestern China using low pressure N2 adsorption and FE-SEM methods. *Mar. Pet. Geol.* **2013**, *48*, 8−19.

(38) Tong, M.; Tao, H. Permeability estimating from complex resistivity measurement of shaly sand reservoir. *Geophys. J. Int.* **2008**, *173*, 733−739.

(39) Wang, Q.; Wang, T.; Liu, W.; Zhang, J.; Feng, Q.; Lu, H.; Peng, P. Relationships among composition, porosity and permeability of

https://doi.org/10.1021/acs.energyfuels.3c00899
Energy Fuels 2023, 37, 7809−7822

Longmaxi Shale reservoir in the Weiyuan Block, Sichuan Basin, China. *Mar. Pet. Geol.* **2019**, *102*, 33−47.
(40) Katti, G.; Ara, S. A.; Shireen, A. Magnetic resonance imaging (MRI)−A review. *Int. J. Dent. Hyg.* **2011**, *3*, 65−70.
(41) Zhang, Q. B.; Zhao, J. A review of dynamic experimental techniques and mechanical behaviour of rock materials. *Rock Mech. Rock Eng.* **2014**, *47*, 1411−1478.
(42) Kate, J. M. Influence of Saturation on Dynamic Elastic Constant of Sandstones. Rock Engineering and Technology for Sustainable Underground Construction. In *Eurock 2012-the 2012 ISRM International Symposium*: Stockholm, Sweden, 2012; pp 28−30.
(43) ASTM. *Standard Test Method for Laboratory Determination of Water (Moisture) Content of Soil and Rock by Mass*; American Society for Testing and Materials: Philadelphia, 1998.
(44) Sing, K. S. Reporting physisorption data for gas/solid systems with special reference to the determination of surface area and porosity (Recommendations 1984). *Pure Appl. Chem.* **1985**, *57*, 603−619.
(45) Lyu, C.; Ning, Z.; Wang, Q.; Chen, M. Application of NMR T 2 to pore size distribution and movable fluid distribution in tight sandstones. *Energy Fuels* **2018**, *32*, 1395−1405.
(46) Chen, G.; Li, C.; Lu, S.; Guo, T.; Wang, M.; Xue, Q.; Zhang, T.; Li, Z.; Sun, Y.; Liu, J.; Jiang, S. Critical factors controlling adsorption capacity of shale gas in Wufeng-Longmaxi formation, Sichuan Basin: Evidences from both experiments and molecular simulations. *J. Nat. Gas Sci. Eng.* **2021**, *88*, 103774.
(47) Gao, F.; Song, Y.; Li, Z.; Xiong, F.; Chen, L.; Zhang, X.; Chen, Z.; Moortgat, J. Quantitative characterization of pore connectivity using NMR and MIP: A case study of the Wangyinpu and Guanyintang shales in the Xiuwu basin, Southern China. *Int. J. Coal Geol.* **2018**, *197*, 53−65.
(48) Zhang, Z.; Yu, Q. The effect of water vapor on methane adsorption in the nanopores of shale. *J. Nat. Gas Sci. Eng.* **2022**, *101*, 104536.
(49) Yang, F.; Zheng, H.; Guo, Q.; Lyu, B.; Nie, S.; Wang, H. Modeling water imbibition and penetration in shales: New insights into the retention of fracturing fluids. *Energy Fuels* **2021**, *35*, 13776−13787.
(50) Kumar, V.; Sondergeld, C.; Rai, C. S. Effect of mineralogy and organic matter on mechanical properties of shale. *Interpretation* **2015**, *3*, SV9−SV15.
(51) Yang, W.; Zuo, R.; Jiang, Z.; Chen, D.; Song, Y.; Luo, Q.; Wang, Q.; Zhu, H. Effect of lithofacies on pore structure and new insights into pore-preserving mechanisms of the over-mature Qiongzhusi marine shales in Lower Cambrian of the southern Sichuan Basin, China. *Mar. Petrol. Geol.* **2018**, *98*, 746−762.
(52) Zhang, W.; Zhang, D.; Zhao, J. Experimental investigation of water sensitivity effects on microscale mechanical behavior of shale. *Int. J. Rock Mech. Min. Sci.* **2021**, *145*, 104837.
(53) Sheng, M.; Tian, S.; Cheng, Z.; Ge, H. Insights into the influence of fluid imbibition on dynamic mechanics of tight shale. *J. Pet. Sci. Eng.* **2019**, *173*, 1031−1036.
(54) Ma, T.; Chen, P. Study of meso-damage characteristics of shale hydration based on CT scanning technology. *Petrol. Explor. Dev.* **2014**, *41*, 249−256.
(55) Anderson, R. L.; Ratcliffe, I.; Greenwell, H. C.; Williams, P. A.; Cliffe, S.; Coveney, P. V. Clay swelling — A challenge in the oilfield. *Earth-Sci. Rev.* **2010**, *98*, 201−216.
(56) Pan, B.; Yin, X.; Iglauer, S. A review on clay wettability: From experimental investigations to molecular dynamics simulations. *Adv. Colloid Interface Sci.* **2020**, *285*, 102266.
(57) Parker, G. G. *Piping: A Geomorphic Agent in Landform Development of the Drylands*; International Association of Scientific Hydrology: Wallingford, UK, 1964; Vol. *65*, pp 103−113.
(58) Morsy, S.; Sheng, J. J. Imbibition characteristics of the Barnett shale formation. In *SPE Unconventional Resources Conference*; OnePetro, 2014.
(59) Li, Y.; Chen, J.; Elsworth, D.; Pan, Z.; Ma, X. Nanoscale mechanical property variations concerning mineral composition and contact of marine shale. *Geosci. Front.* **2022**, *13*, 101405.

https://doi.org/10.1021/acs.energyfuels.3c00899
Energy Fuels 2023, 37, 7809−7822